Simulation of scattering and phase behavior around the isotropic–nematic transition of discotic particles

Journal of Colloid and Interface Science 377 (2012) 94–104

Contents lists available at SciVerse ScienceDirect

Journal of Colloid and Interface Science

www.elsevier.com/locate/jcis

Simulation of scattering and phase behavior around the isotropic–nematic transition of discotic particles

Rui P.S. Fartaria [1], Nadeem Javid, Jan Sefcik, Martin B. Sweatman *

Department of Chemical and Process Engineering, University of Strathclyde, 75 Montrose Street, Glasgow G1 1XJ, United Kingdom

ARTICLE INFO

Article history:
Received 21 December 2011
Accepted 14 March 2012
Available online 28 March 2012

Keywords:
Cut-sphere
Algorithm
Isotropic
Nematic
Phase transition
SAXS
Light scattering
Clay
Monte Carlo
Umbrella sampling
Structure factor
Nanocomposite
Dispersion
Discotic

ABSTRACT

The detailed study of the isotropic–nematic phase transition in a system of discotic particles of aspect ratios $L/D \leqslant 0.1$ presented here is relevant to a broad range of colloidal suspensions of chemically modified clay particles. Using Monte Carlo simulation techniques the equation of state, radial distribution functions, structure factors and normalized scattering intensities are calculated for each phase. The results are interpreted and related to previously reported free energy calculations [Fartaria and Sweatman, Chem. Phys. Lett. 478 (2009) 150], suggesting a nearly continuous isotropic–nematic transition for lower aspect ratios. Given this behavior we examined the structural information for each phase to determine how experimental scattering data might be used to distinguish the two phases. The radial distribution functions in each phase depend strongly on aspect ratio, and for larger aspect ratios a dramatic increase in the local ordering of discotic particles (represented here as cut-spheres) is observed just before the phase transition. However, this nearest-neighbor ordering seen in $g(r)$ around $r/D = 0.1$ would hardly be discernible in experimental scattering data subject to usual statistical errors. The structure factors and scattering intensities were calculated for $L/D = 0.1$, 0.04 and 0.01 for the isotropic and nematic phases at and away from the isotropic–nematic transition. While the isotropic–nematic phase transition can be detected from the height and shape of the first scattering peak around $7QD$ for larger aspect ratios, this feature becomes much less discriminatory with decreasing aspect ratio. Instead, scattering intensities at low scattering vector amplitudes ($Q \to 0$) can be used for detection of the phase transition at low aspect ratios. These results provide useful insight to guide interpretation of X-ray and light scattering measurements for colloidal dispersions of thin platelets undergoing isotropic–nematic transitions.

1. Introduction

Suspensions of clay particles dispersed in polymerizable solvents can be used in the synthesis of nano-composite materials with remarkably enhanced properties such as gas permeability, heat conductance, biodegradability, improved thermal stability and mechanical properties [1–4]. Another system of interest, with potential for nanotechnology applications [5], is the case of dispersions of graphene sheets in organic [6–8] or polar solvents [9]. It is important to understand how the structure of these materials can be controlled so that their properties can be fine-tuned for specific applications. The special feature of these systems is the discotic character of their nanoparticles, which gives rise to the potential for forming a range of discotic liquid crystal phases within nanocomposite materials. In this work we are particularly interested in the nematic phase of such systems, since in this phase the particles are aligned such that they form a very good barrier against diffusion in any resulting nanocomposite material. If this phase can be encouraged to form in these materials at high concentrations, such that all particles are aligned parallel with the material's surface, as opposed to forming microdomains with randomly distributed orientations, then a continuous barrier material, or barrier film, can be produced. The barrier properties of such a highly ordered material would far exceed those of existing analogous materials. For such phases to form, the dominant inter-particle interaction should be equivalent to hard-core exclusion, i.e. attractive interactions need to be suppressed. However, for many discotic nanoparticles, including clays, this regime normally occurs only at sufficiently high temperatures, where thermal energy is much greater than attractive interaction energies. The focus of this work, then, is on the isotropic–nematic phase transition of hard-core discotic particles with aspect ratios corresponding to clays of various kinds. We neglect attractive interactions altogether in our models, and hence our work essentially corresponds to the high temperature limit of discotic nanoparticle dispersions. In recent years there have been several theoretical and experimental studies of discotic colloidal dispersions. From a theoretical perspective several

* Corresponding author.
E-mail address: martin.sweatman@strath.ac.uk (M.B. Sweatman).
[1] Present address: REQUIMTE, Departamento de Química, Faculdade de Ciências da Universidade do Porto, Rua do Campo Alegre, s/n, 4169-007 Porto, Portugal.

0021-9797/$ - see front matter © 2012 Elsevier Inc. All rights reserved.
http://dx.doi.org/10.1016/j.jcis.2012.03.046

different modeling approaches have been used. Usually, regardless of which model and method is used, the solvent degrees of freedom are 'integrated out', leaving just the discotic colloids which interact via an effective solvent mediated potential. This technique is described in a formal sense by Dijkstra et al. [10]. Early models used in simulations of these systems represent colloidal particles by a finite set of spherical particles connected in a disk shape [11,12], others use analytical potentials able to describe different degrees of anisotropy [13]. However, the more usual and simple models are based on solid hard cores that describe the shape of the particles. This is the case of the cut-sphere model, initially used by Veerman and Frenkel [14] to study the phase diagram of discotic systems with a range of aspect ratios, specified by L/D (thickness over diameter), between 0.1 and 0.4. Previous simulation studies [15] also investigated the isotropic–nematic (I–N) transition of infinitely thin disks which are a limiting case of the cut-sphere system. Bates and Frenkel [16,17] further extended the study of the I–N transition for systems of polydisperse disks (in diameter) and for disks with different geometrical shapes. Regarding the I–N transition, the general conclusion of these studies is that discotic systems (based on the cut-sphere model) all present a weak first order I–N transition up to aspect ratios of $L/D \sim 0.15$. For thicker disks the nematic phase was found to be unstable (throughout the text "thin" or "thick" refer to thickness relative to diameter). Veerman and Frenkel studied more dense phases, including columnar and crystalline, finding also a new phase, the so called cubatic phase, in which the disks are arranged in small stacks with three dimensional ordering along three perpendicular axes.

Other theoretical methods have also been applied to discotic systems. Density functional theory (DFT) and integral equation theories (IETs) have been applied to infinitely thin disks and cut-spheres. A study of the cut-sphere system based on the Hypernetted Chain (HNC) closure presented by Chamoux and Perera [18]. was able to locate the I–N transition in reasonable accordance with simulation results and could also predict the formation of the cubatic phase. However, the corresponding results for the equation of state are in good agreement with simulation only for the low-density part of the isotropic phase. Using high-order virial expansions, You et al. [19] present another study on the equation of state of discotic systems (among others). This approach also yields good results for the isotropic low density states but becomes more inaccurate at densities close to the I–N transition. Esztermann et al. [20] apply DFT and fundamental measure theory (FMT) to study the I–N transition of infinitely thin disks and determine the coexistence properties at the transition, in particular the densities and the value of the nematic order parameter in the nematic phase, in good agreement with simulation results from Frenkel and Eppenga [15]. In a more recent work, using simulation, FMT DFT and IET, Cheung et al. [21,22] study the isotropic phase of a variety of hard-particle liquids, with emphasis on hard platelets. Although these methods are successful in describing the equation of state at lower densities, they are found to be less successful for platelet based systems at higher densities.

Despite this earlier work there is little detailed information about the nature of the I–N transition or the structural properties of each phase for a wide range of aspect ratios. Structural characterization of colloidal suspensions is experimentally accessible through scattering methods, such as small angle X-ray scattering (SAXS) and static light scattering (SLS), which have been widely used to identify structural features of various phases [23,24] as well as to compare measured scattering intensities with detailed structural information obtained from simulations [25,26]. So the aim of this present work is to provide this kind of detailed information about the I–N transition to complement experimental studies on dispersions of platelet based systems. In particular, we are interested in the nature of the transition and the structure of each phase. On the one hand, this information will help to verify the existence of each phase in some real dispersions by making suitable experimental measurements. On the other hand, experimental measurement of structural data can help to parametrize simulation models. Ultimately, this information should be useful for the design of nanocomposite materials with specific morphologies tailored for particular applications.

We choose to model colloidal platelets in terms of the cut-sphere model with aspect ratios $L/D \leqslant 0.1$ and use Monte-Carlo simulation techniques to analyze their properties. Although earlier simulation work has examined some properties of this system for aspect ratios 0.0 and 0.1, there is almost no data available for other aspect ratios which correspond, for example, to dispersions of commonly available organically modified clay platelets, e.g., Montmorillonite ($L/D \sim 0.005$) [27,4], Laponite ($L/D \sim 0.04$) [28,29] and Gibbsite ($L/D \sim 0.07$). In the case of Gibbsite, some simulation results have already been presented by van der Beek et al. [30] that show qualitative agreement with experimental results for the relative location of the isotropic–nematic and nematic-columnar phase transitions. The cut-sphere model represents a reasonable geometrical approximation of colloidal clay particles, while hard-core exclusion corresponds to some experimental model systems such as organically modified Gibbsite suspended in toluene, investigated previously [31]. It can be expected that hard-core exclusion is the most important interaction between platelets determining their short-range ordering, and it certainly dominates in the high temperature regime. By adopting this model, additional interactions, such as electrostatic and dispersion, are considered to be negligible. The paper is organized as follows. In Section 2 we present the model and simulation details, while in Section 3 we present results for the equation of state, the location and nature of the I–N transition, and distribution functions, structure factors and scattering intensities for several aspect ratios. This is followed by a summary and final remarks in Section 4. For convenience, in Appendix A we present the formulation of the algorithm used for the detection of cut-sphere geometrical overlapping.

2. Methodology

2.1. Cut-sphere model

A cut-sphere is a geometrical object constructed by the intersection of a sphere with two parallel planes equidistant from the sphere center, as depicted in Fig. 1. The natural descriptors for a cut-sphere are the thickness, L, the diameter, D, and the director vector, $\mathbf{n}$. In order to be able to use this model in simulations one has to develop an algorithm for deciding when a pair of particles are overlapping with each other. Our algorithm is equivalent to the one from Allen et al. [32] and is presented in detail in Appendix A. The algorithm was tested primarily by generating millions of random configurations of pairs of particles and plotting the intersection of the two objects using graphical software. Each result, overlap or no-overlap, was then compared with the result given

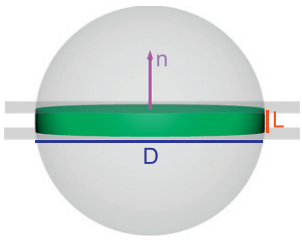

Fig. 1. Cut-sphere object and respective descriptors: thickness, L, and diameter, D; $\mathbf{n}$ is the unit director vector perpendicular to the faces.

by the algorithm. In order to further test the algorithm, the same strategy was applied to accepted and rejected configurations extracted from Monte Carlo (MC) simulations with 288 cut-spheres.

2.2. General details of MC simulations

Systems of 288 and 2048 cut-spheres were used in the Monte Carlo simulations. For the smaller systems, the averages were taken over longer simulations up to 10^6 MC moves per particle. A MC move consisted of a trial translation and a trial rotation, performed independently. For the larger system the averages were taken from runs of up to 2×10^5 MC moves per particle. Standard cubic periodic boundary conditions [33] were used in all simulations. The equation of state was calculated using both canonical (NVT) and isothermal-isobaric (NpT) ensembles. Simulations for the calculation of free energy profiles were performed using an umbrella-sampling technique and an NpT ensemble.

2.3. Pressure calculation

For the calculation of pressure with the NVT ensemble, the so called "Virtual–Volume–Scaling" method, as presented by Frenkel and Eppenga [15] and further developed by Harismiadis et al. [34], was used. A more recent study on the effectiveness of the method is presented by de Miguel and Jackson [35]. With this method, small virtual random compressions or expansions of the system are performed during the simulation. The basis of the method is the relation between pressure and the Helmholtz free energy:

$$p = -\left(\frac{\partial F}{\partial V}\right)_{N,T} = -\lim_{\Delta V \to 0} \frac{F(V+\Delta V) - F(V)}{\Delta V} \tag{1}$$

where p is the pressure, F is the Helmholtz free energy, V is the volume, N is the number of particles and T is the temperature. By expressing F in terms of the canonical partition function Q_{NVT}, i.e.

$$-\beta F = \ln\ Q_{NVT} = \frac{1}{\Lambda^{3N} N!} \int \mathrm{d}r^N \exp(-\beta U(r^N)) \tag{2}$$

where $\beta = 1/k_B T$ with k_B as the Boltzmann's constant, Λ is the de Broglie thermal wavelength and U is the configurational part of the Hamiltonian of the system (which depends on the configuration of the N-particle system, denoted r^N), one can write that for two systems at the same temperature but with different volumes, V and $V' = V + \Delta V$:

$$-\beta[F(V') - F(V)] = \ln \left\langle \left(1 + \frac{\Delta V}{V}\right)^N \exp(-\beta \Delta U) \right\rangle_V \tag{3}$$

where $\Delta U = U(r^N, V') - U(r^N, V)$ is the change in configurational energy due to the change in volume. The subscript V in the ensemble average means that the average is taken for configurations of the system with the original volume. After some convenient rearrangements of Eq. (3) and using the definition in Eq. (1) we get that the pressure can be calculated from

$$\beta p = \rho \left[1 - \frac{1}{V} \lim_{\Delta\rho \to 0} \frac{\ln\langle \exp(-\beta \Delta U)\rangle}{\Delta \rho}\right] \tag{4}$$

where $\Delta\rho$ is the change in density. For systems with hard-interactions, only virtual compressions are used, because $\Delta U = 0$ for any expansion. For this kind of system Eq. (4) becomes

$$\beta p = \rho \left[1 - \frac{1}{V} \lim_{\Delta\rho \to 0^+} \frac{\ln(P_{acc})}{\Delta \rho}\right] \tag{5}$$

with $P_{acc} = \langle \exp(-\beta \Delta U)\rangle$ being the probability of a small random virtual compression not resulting in an overlap when $\Delta\rho > 0$. During the simulation a histogram for $P_{acc}(\Delta\rho)$ is built. For small changes in density we can approximate $\ln(P_{acc}) \sim -\alpha \Delta\rho$. Performing a linear regression yields the pressure

$$\beta p = \rho\left(1 + \frac{\alpha}{V}\right). \tag{6}$$

2.4. Nematic order parameter

The nematic order parameter, S, has a value close to zero for the isotropic phase and close to one for the nematic phase. The nematic order parameter can be calculated from the largest eigenvalue of the nematic tensor order parameter. This is a traceless tensor defined as

$$\mathbf{Q} = \frac{1}{N} \sum_{i=1}^{N} \left(\frac{3}{2} \mathbf{n}_i \mathbf{n}_i - \frac{1}{2} \mathbf{I}\right) \tag{7}$$

where $\mathbf{I}$ is the 3×3 identity tensor and $\mathbf{n}_i$ $\mathbf{n}_i$ is the vector direct product of the director vectors of the cut-spheres. This tensor has three eigen values λ_+, λ_0 and λ_-. In the works of Veerman and Frenkel [15,14] $S = -2\lambda_0$ was used as the nematic order parameter because of the drastic change of this parameter from nearly zero to almost 1 through the I–N transition. In this work we opt for the more usual [15] value of $S = \lambda_+$.

2.5. Umbrella-sampling

Umbrella-sampling [33] simulations and the NpT ensemble were used to calculate the dependence of the free energy on the nematic order parameter. During a simulation, the system was constrained to configurations with specific values of the nematic order parameter, S_i, where the index i indicates the ith umbrella simulation. The bias potential used for this effect was, $\Phi(S) = k(S - S_i)^2$, with $k = 10^4$. The nematic order parameter interval [0, 1] was divided into 100 partially overlapping windows and a simulation was performed for each value S_i. In each simulation a histogram was built for the quantity $\langle \delta[S - S_i]\rangle$ and the free energy was calculated for the ith window using

$$-\beta G_i(S) = \beta \Phi(S) + \ln(\langle \delta[S - S_i]\rangle). \tag{8}$$

The free energy profiles calculated in each window differ, to within statistical error, by a constant term. To obtain the complete curve for $-\beta G(S)$ each curve $-\beta G_i(S)$ was fitted with a third order polynomial using linear regression methods. A new curve was constructed using the derivatives of the fitted polynomials. In order to smooth the derivatives curve, the overlapping regions, if any, of the individual derivative curves were averaged. Subsequently, the derivatives curve was integrated thus regenerating the complete curve for $-\beta G(S)$ to within a constant.

3. Results

3.1. Equation of state and order parameter

To validate the cut-sphere model used in this work the equation of state for both the isotropic and nematic phases for $L/D = 0.1$ was reproduced (see Fig. 2a) using a system of 288 cut-spheres and the NVT ensemble. The calculations were repeated using the NpT ensemble. The average nematic order parameter was calculated for each pressure/density point for both ensembles as presented in Fig. 2b. Our result for the equation of state matches quite well with that of Veerman and Frenkel and with that of Piñeiro et al. [36] for the isotropic and nematic phases. At the transition there is a small difference in density and pressure with the result of Veerman and Frenkel, but that can be ascribed to the length of the simulations, which was of ~50,000 MC moves per particle in their work and $\sim 10^6$ in this work. Additional calculations were

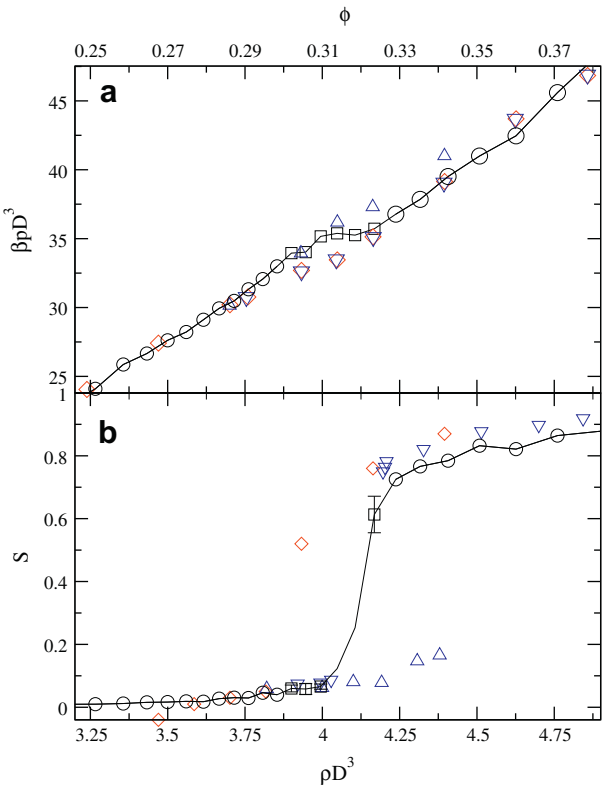

Fig. 2. Data obtained for cut-spheres with aspect ratio $L/D = 0.1$. (a) Equation of state in the vicinity of the isotropic–nematic transition: *NVT* from this work (black circles and squares), *NVT* results from Veerman and Frenkel (red diamonds) and *NpT* results from Piñeiro et al. (blue – triangles up for compression and triangles down for expansion). (b) Nematic order parameter dependence on the density (colors and symbols are the same as in (a)). (For interpretation of the references to color in this figure legend, the reader is referred to the web version of this article.)

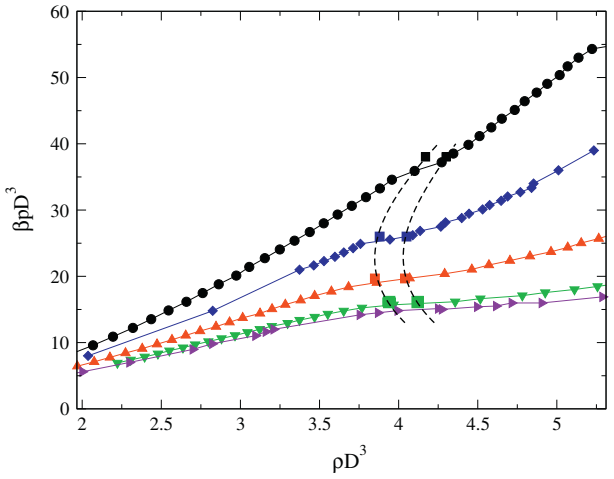

Fig. 3. Equation of state for aspect ratios $L/D = 0.1$ (black), 0.07 (blue), 0.04 (red), 0.01 (green) calculated in this work and for infinitely thin disks (violet) taken from the work of Bates and Frenkel. The squares correspond to the *I–N* phase equilibrium densities, calculated in this work, from free energy calculations (see Section 3.2) and the dashed lines are guides showing the density minima effect found for intermediate L/D values. Full lines are also guides for the eye. (For interpretation of the references to color in this figure legend, the reader is referred to the web version of this article.)

made with a system of 2048 cut-spheres to check for finite size effects. No significant effects were found for the equation of state at the chosen points.

Fig. 2b displays results for the dependence of the nematic order parameter with density. Our results for the transition location are in good agreement with those of Piñeiro et al. However, they claim that the difference between their results (and hence ours) and those of Veerman and Frenkel for the nematic order parameter are due to the number of particles used in their simulations ($N = 1500$). As we used only 288 particles and obtained very similar results the differences should be attributed to the length of the simulations, which were of the order of 10^6 steps per particle in the present and Piñeiro et al. [36] studies and 10^4 for the one from Veerman and Frenkel [14]. Indeed, during our simulations, systems with densities between $\rho D^3 = 3.8$ and 4.2 sample both high and low values of S with the average values being shown as squares on Fig. 2. This reinforces the importance of long runs to sufficiently explore phase space. It is expected that for larger systems the absolute free energy barrier between the two phases becomes larger and some hysteresis could be found as, in fact, Piñeiro et al. have found in their simulations. We should note that the small, systematic, difference between values of S on the nematic phase side are due to the different definitions of the order parameter, as referred above.

By analysing the data presented in Fig. 2, it is possible to approximately determine the location of the *I–N* phase transition. Using the criteria that $S_I < 0.1$ for the isotropic phase and $S_N > 0.6$ for the nematic phase we find that the *I–N* transition is located at ($\rho_I D^3 \sim 3.9$; $\rho_N D^3 \sim 4.2$; $\beta p_{I-N} D^3 \sim 35$). Using similar criteria ($S_N \sim 0.3$), Veerman and Frenkel found ($\rho_I D^3 \sim 3.82$; $\rho_N D^3 \sim 3.87$). Using Gibbs-ensemble simulations Piñeiro et al. determine the coexistence densities to be ($\rho_I D^3 \sim 4.11$; $\rho_N D^3 \sim 4.26$;). The agreement between these values is relatively good as these are only tentative values based on the assumption that the nematic order parameter has those values at the *I–N* transition.

We made further calculations, using 288 and 2048 cut-spheres, for the equation of state, nematic order parameter and *I–N* transition location for aspect ratios of $L/D = 0.07$, 0.04 and 0.01, which are relevant for some commonly available clay dispersions. In Fig. 3 we present the equations of state of cut-spheres for those aspect ratios. For clarity, we also include, in the same picture, the equilibrium densities at the *I–N* transition calculated via umbrella sampling (this technique will be described in the next section). The data for infinitely thin disks, taken from Bates and Frenkel [17], is also presented as a limiting case. Clearly, the behavior of particles with $L/D = 0.01$ is already very close to that of infinitely thin particles.

We see from Fig. 3 that the equation of state becomes flatter for increasingly thin particles, i.e. the compressibility increases significantly with decreasing aspect ratio in the region of the *I–N* transition. As a result, the coexistence pressure reduces with decreasing aspect ratio. Interestingly, the nematic phase, although more dense, always has a higher compressibility than the isotropic phase at the transition. This effect also increases with decreasing aspect ratio and it is remarkably strong for the case of infinitely thin disks where the compressibility of the nematic phase is almost three times that of the isotropic phase. This is interpreted as a consequence of the orientational correlations in this phase that are thought to enable easier compression of the system, particularly in the direction parallel to the nematic director.

However, the preceding discussion concerning the location of the transition ignores the effect of finite-size effects. Analysing the equations of state, for 288 and 2048 cut-spheres, we did not find any significant finite size effects away from the *I–N* transition. The importance of finite size effects only became clear when we performed free energy calculations at the transition as will be discussed in the next section. Bates and Frenkel [17] verified, in a study of infinitely thin disks, that finite size effects were important

close to the *I–N* transition. It follows that it is only possible to decide the location of the *I–N* transition using the nematic order parameter for higher aspect ratios, where the jump in S is sharp and strong. For smaller aspect ratios fluctuations in the nematic order parameter become increasingly large as the transition is approached from either side. At the same time, the average value of S in the nematic phase varies from ~0.8 to ~0.4 for aspect ratios of 0.1 and 0.01, respectively. It is therefore difficult to confidently ascertain the value of S for the nematic phase in equilibrium with the isotropic phase for small aspect ratios. To deal with this difficulty we used a free energy method (umbrella sampling) that allows a more accurate determination of the location of the transition. Results are presented in the next section.

3.2. Free energy profiles

We used a free energy based method to accurately determine the coexistence properties at the *I–N* transition. By performing umbrella sampling simulations with the NpT ensemble we calculated the free energy dependence on the nematic order parameter for the three aspect ratios mentioned above. The results of these calculations were communicated in a previous publication [37], but are very important for the interpretation of the equation of state, and structural changes, at the *I–N* transition. Therefore, a summary of that work is given here.

The calculations were very sensitive to the thermodynamic conditions imposed on the system. That is, very small changes to the pressure resulted in free energy profiles that unequivocally favored one of the phases. The free energy wells are much broader for the smaller aspect ratios indicating that large fluctuations of the nematic order parameter can occur. Furthermore, the free energy barrier for the smaller aspect ratios is extremely small. Indeed, we could not be completely confident that a free energy barrier exists at all for $L/D \leqslant 0.04$, and hence we cannot rule out the existence of a critical point for $L/D \leqslant 0.04$. This is in complete agreement with what was observed during the NpT and NVT simulations when determining the equation of state. From the location of the minima (or apparent minima) we determined the nematic order parameter for each phase and the respective coexisting densities. The relevant thermodynamic properties at the *I–N* transition are summarized in Table 1. The *I–N* transition densities were overlapped in Fig. 3 in order to clarify the location of the *I–N* transition in the equation of state. The nematic order parameter at the *I–N* transition shows a strong dependence on the aspect ratio, particularly for the nematic phase, confirming that indeed it is not possible to use solely the equation of state and the jump in the nematic order parameter for an accurate determination of the *I–N* transition. All the properties at the transition show a consistent monotonous dependency on the aspect ratio, except density for which we detected a minimum close to $L/D \sim 0.04$ (see Fig. 3 – dashed line). We interpreted this phenomenon as the competition between the dependence of solid volume and free volume on aspect ratio. The free volume dependency on aspect ratio can be related to pre-nematic ordering in the isotropic phase at the transition (see our earlier work for a discussion of this). By analysing the probability of occurrence of nematic domains it is found that thicker disks tend to form a larger number of short range nematic structures and that thinner disks tend to form fewer large (longer range) nematic domains. Hence, we suggest that the free energy barrier for the *I–N* transition is related to the number of separate nematic-like domains required to spontaneously align to form a nematic phase. Indeed, for the thinner aspect ratios the free energy barrier is so small that it might be possible to observe behavior similar to critical opalescence [38]. That is, when samples where a nematic phase is present, away from the *I–N* transition, are illuminated with polarized light (observed in cross-polarizer) normal birefringence [39–42,29] would be observed but at the *I–N* transition this would turn to a kind of diffused birefringence. From the free energy barrier one can also draw some conclusions about the interfacial tension (γ) between the two phases. In fact, γ, is proportional to the free energy barrier, by $\gamma = F/(2L^2)$, where L is the length of the simulation box, and can be estimated from simulations using finite size scaling methods [43] where γ is extrapolated for $L \to \infty$. This would be a study on its own and it is beyond the scope of the presented work. Nevertheless, we can conclude, from our results on the evolution of the free energy barrier, that the interfacial tension will be much higher between the isotropic and nematic phases of platelets with higher aspect ratio.

3.3. Radial distribution functions

The radial distributions of the isotropic and nematic phases close and far from the transition complement the thermodynamic information of the previous section. Moreover, these distributions can be transformed to structure factors and used to predict scattering intensities that can be directly compared with experimental data. We present the evolution of the radial distribution function (RDF) for both isotropic and nematic phases, for the three aspect ratios 0.1, 0.04 and 0.01, in Fig. 4. The detailed RDF plots correspond to isotropic and nematic phases both close and far from the transition while the insets show the surface plots for the complete density range and interpolate the RDFs at intermediate densities. Please note that the serrated edge visible on some parts of the sharp peak at one diameter is an artifact of the triangulation algorithm of the plotting software and should be regarded instead as a smooth edge. The selected RDFs (close and far from transition) were calculated for the 2048 cut-spheres system using NVT or NpT calculations (they match perfectly) and are presented together with the RDFs taken from the umbrella sampling simulations (NpT) corresponding to the free energy minima visible in Fig. 3 (dashed line). In the bottom part of Fig. 4 we present snapshots of randomly selected configurations for the isotropic and nematic phases at the phase transition (corresponding to free energy minima of Fig. 3). These clarify the interpretation of the RDFs and, also,

Table 1
Results for the *I–N* transition with cut-spheres of different aspect ratios. PIN is the percentage of particles considered to be parallel in the nematic phase (see text).

L/D	S_I	S_N	$\beta\Delta\mu \times 10^3$	$\rho_I D^3$	$\rho_N D^3$	$\beta p D^3$	PIN (%)
0.1	0.08 ± 0.02	0.83 ± 0.02	9 ± 2	4.17 ± 0.01	4.30 ± 0.01	38.2 ± 0.25	73
Veerman and Frenkel [14]				3.82	3.87		
Piñeiro et al. [36]				4.11	4.25		
0.04	0.14 ± 0.04	0.47 ± 0.04	0.5 ± 0.2	3.85 ± 0.02	4.04 ± 0.02	19.6 ± 0.1	30
0.01	0.11 ± 0.04	0.44 ± 0.04	0.5 ± 0.2	3.94 ± 0.02	4.12 ± 0.02	16.1 ± 0.1	30
0.0							
Frenkel and Eppenga[15]		0.37		3.78	4.07		
Bates and Frenkel [17]				3.68 ± 0.02	3.98 ± 0.05		
Esztermann et al. [20]		0.49		3.34	3.68		

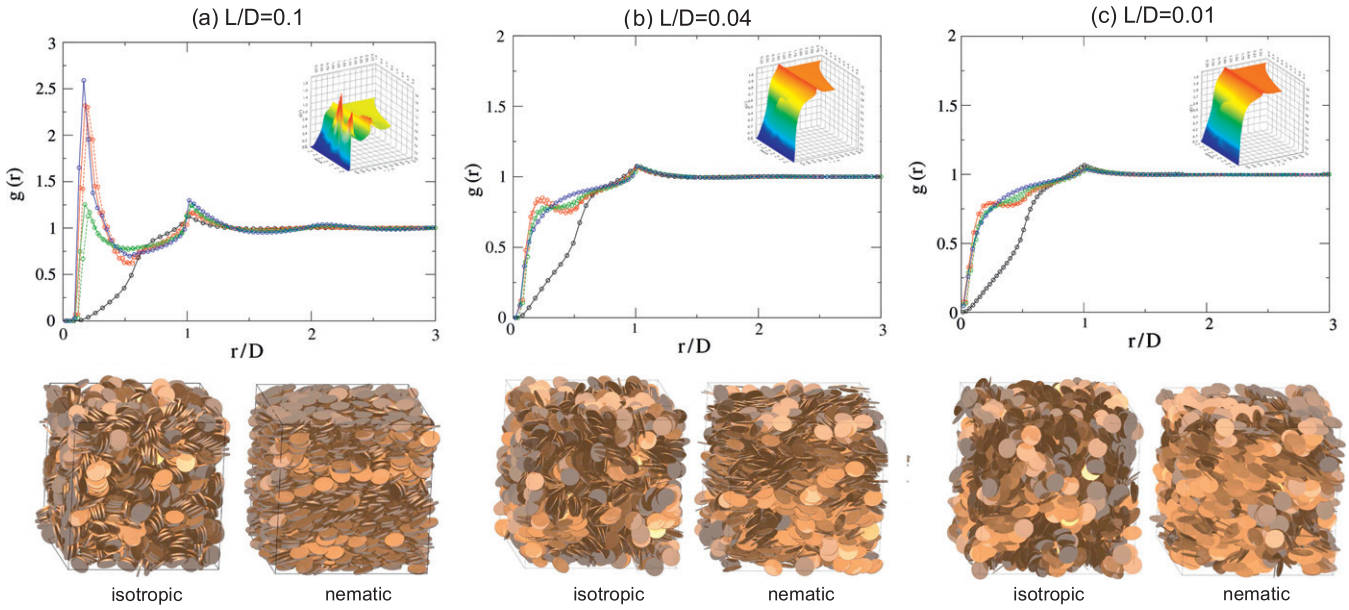

Fig. 4. Radial distribution evolution with density for cut-spheres with aspect ratio L/D = 0.1, 0.04 and 0.01. Top (plots): black – isotropic phase at low density; red – isotropic phase at I–N transition; green – nematic phase at transition; blue – nematic phase at high density. Dashed lines correspond to the RDFs from the constrained system at the free energy minima from previous calculations [37]. The insets show the surface plots for the full evolution of the RDF through the I–N transition. The densities and solid volume fractions (in brackets), $\rho D^3(\phi)$, are: (a) 1.3 (0.10), 4.2 (0.33), 4.3 (0.34) and 5.1 (0.40); (b) 1.5 (0.05), 3.8 (0.12), 4.1 (0.13) and 5.1 (0.16); (c) 1.7 (0.013), 3.9 (0.031), 4.3 (0.034) and 5.1 (0.040). Bottom (snapshots): randomly selected configurations for the isotropic and nematic phase at the phase transition. (For interpretation of the references to color in this figure legend, the reader is referred to the web version of this article.)

clearly show the columnar ordering of thicker platelets and the formation of nematic domains on the isotropic phases of thicker and thinner platelets, respectively, at the phase transition. The RDFs display the same general characteristics observed in previous work with cut-spheres of L/D = 0.1 and infinitely thin disks. For all aspect ratios we find a sharp peak positioned at $r/D \sim 1$. We use this peak to divide the RDF in two main regions. The first is on the left of the peak ($r/D < 1$) and corresponds to separations within which disks can touch. The second is to the right of the peak ($r/D > 1$) and corresponds to longer range correlations. This part of the RDF shows a smooth, sometimes oscillatory, variation towards unity for all aspect ratios. In the first region ($r/D < 1$) we find a marked dependence of the shape of the RDF with aspect ratio. For all aspect ratios, at low density, $g(r)$ increases smoothly, in the range $L/D < r/D < 1$, from zero to the peak at $r/D = 1$. For the smaller aspect ratios, as density increases, a uniform band starts to grow in intensity and when reaching the density of the I–N transition this band is always more intense in the nematic phase than in the corresponding isotropic phase. For $L/D > 0.04$ we see the development of a peak in the isotropic phase, at $r/D \sim 0.2$, as the system approaches the I–N transition. The intensity of this peak increases dramatically with aspect ratio so that at $L/D = 0.1$ the isotropic phase at the I–N transition presents a very intense peak at $r/D \sim 0.2$. This means that as the disks get thicker there is an increased short range "caging" effect due to nearest neighbors. Furthermore, this caging effect disappears for the nematic phase in equilibrium with the isotropic phase. For this phase the peak falls to an intensity equivalent to the one observed at $r/D \sim 1.0$. This freedom of arrangement of particles is interpreted as a consequence of increased orientational correlations in the nematic phase which allow the particles to move in directions perpendicular to the nematic director. This "caging" effect in the isotropic phase effectively increases the number of close neighbors ($r/D < 1$) for thicker particles. This can be better seen by calculating the number of neighbors as a function of distance,

$$N(r) = 4\pi\rho \int_0^r g(r)\, r^2\, dr \tag{9}$$

where ρ is the density, r is the distance and $g(r)$ is the radial distribution function. The results are presented in Fig. 5. At a distance of $r/D \sim 1.0$ all aspect ratios present a number of neighbors between 15 and 16, always with the nematic phase having a slightly larger value (plus ~0.7 neighbors). Between $r/D \sim 1.0$ and ~0.6 this behavior is essentially maintained but for $r/D < 0.6$ the isotropic phase of larger aspect ratio particles clearly presents a larger number of neighbors than the corresponding nematic phase. This effect is very

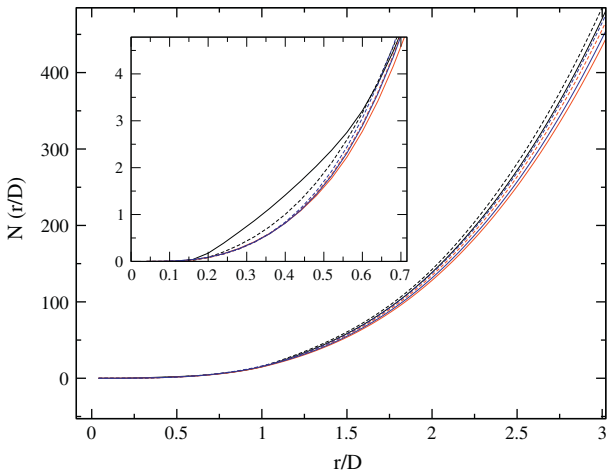

Fig. 5. Variation of the cumulative number of neighbors with distance for different aspect ratios (L/D): black – 0.1; red – 0.04; blue – 0.01. Full lines correspond to the isotropic phase and dashed lines to the nematic phase, both at I–N coexistence. The inset shows the region of $r/D < 0.7$ in detail. (For interpretation of the references to color in this figure legend, the reader is referred to the web version of this article.)

weak for the 0.04 aspect ratio and could only be detected at distances $r/D < 0.3$ and for the aspect ratio of 0.01 it is negligible. At a distance $r/D = 0.6$ the number of neighbors for the isotropic and nematic phases of the system with $L/D = 0.1$ is around three. The main difference is that in the isotropic phase the positions of these neighbors are much more constrained, mainly at $r/D \sim 0.2$. This complements the analysis of nematic-like domains (which include stacks) made in the previous work [37]. Essentially, particles of aspect ratio $L/D = 0.1$ form a large number of small stacks in the isotropic phase in equilibrium with the nematic phase. The transition to the nematic phase is then made through realignment of these small stacks and the breaking of the "caging" effect. This stacking is minimal for particles with aspect ratio $L/D < 0.04$ where the transition is made through the realignment of larger nematic domains.

It is important to note that features in the region $r/D < 1$ would normally be difficult to discern in experimental data subject to the usual experimental and instrumental uncertainties (see the next section below). This is due to the nature of the mathematical transformation between $g(r)$ and $S(q)$, where small distances r correspond to large Q values for which scattering intensities are generally low and any features are often obscured by experimental error. Indeed, the main features of the structure factor $S(q)$ primarily reflect the behavior of $g(r)$ around the sharp peak around $r/D = 1$ and at larger values of r, which as we have already said tends smoothly to unity and so is also relatively featureless. It therefore becomes important to examine static structure factors and intensities which are obtained directly in experiments without any Fourier transformation.

3.4. Structure factors and scattering intensities

The radial distribution functions discussed above were used to calculate the structure factors and normalized scattering intensities for systems of cut-spheres of aspect ratios $L/D = 0.1$, 0.04 and 0.01. These can be used to compare with intensity profiles from scattering experiments (specifically from small angle X-ray scattering, SAXS, and static light scattering, SLS) of the isotropic and nematic phases in dispersions of platelets with various aspect ratios. The static structure factor is related to the radial distribution function by a sine Fourier transform [38,44]

$$S(Q) = 1 + 4\pi\rho\, Q^{-1} \int_0^{\infty} [g(r) - 1]\, r\, \sin(Qr)\, dr \tag{10}$$

where S is the static structure factor, ρ is the number density and Q is the scattering vector amplitude. Having calculated the structure factor, the scattering intensity (normalized by particle concentration) is given by

$$I(Q) = S(Q) \cdot P(Q) \tag{11}$$

where I is the scattering intensity and P is the form factor. The form factor is the scattering intensity from a single platelet and is given by [44,45]

$$P(Q) = Cv^2 \int_0^{\pi/2} \left\{ \frac{\sin[QL\cos(\beta)/2]}{QL\cos(\beta)/2} \right\}^2 \left\{ \frac{2J_1[QD\sin(\beta)/2]}{QD\sin(\beta)/2} \right\}^2 \times \sin(\beta)\, d\beta \tag{12}$$

where C is a constant related to the scattering properties of the platelets and the medium, v is the volume of one platelet (e.g., cut-sphere), L and D are the platelet thickness and diameter, respectively, J_1 is the first order Bessel function and β is the angle between the platelet axis (director vector) and the scattering vector, Q. In Fig. 6 we show the structure factors for the isotropic and nematic phases of cut-spheres, of aspect ratios $L/D = 0.1$, 0.04 and 0.01, both away from and at the I–N transition. These were calculated from the

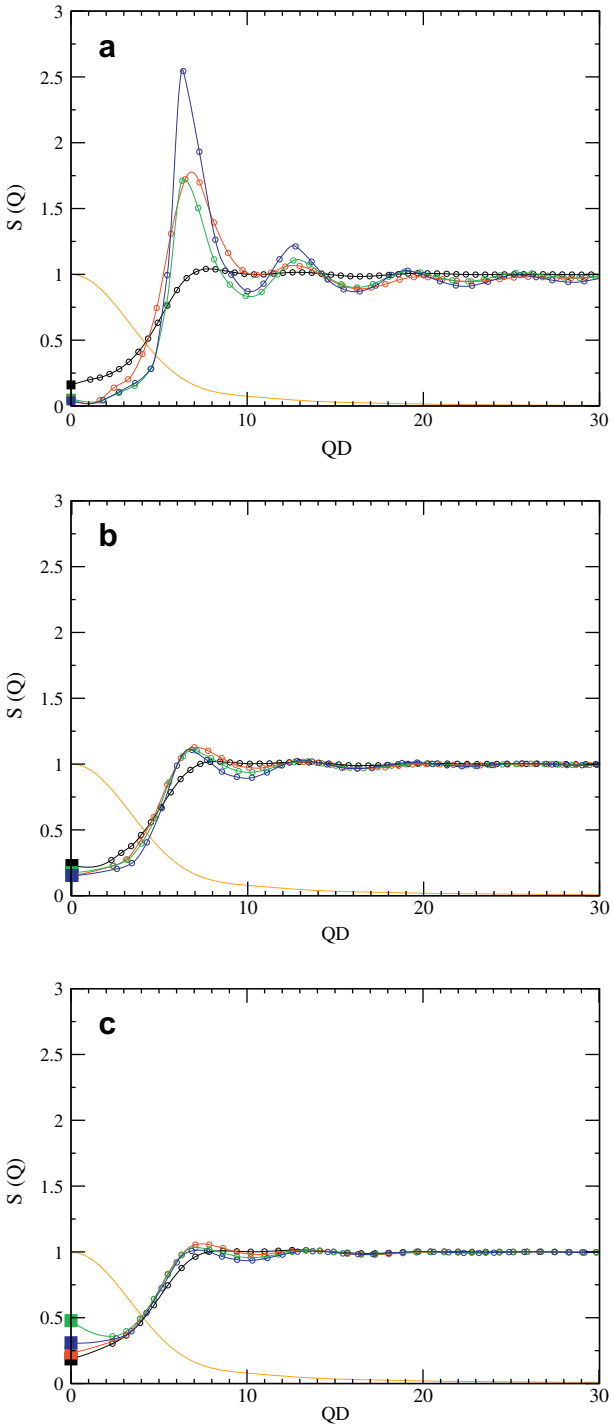

Fig. 6. Structure factors for aspect ratios $L/D = 0.1$ (a), 0.04 (b) and 0.01 (c). Color codes and densities correspond to the ones presented in Fig. 4. The form factor for each aspect ratio is represented by the orange line. Squares correspond to the limits for $S(Q = 0)$ calculated from the equations of state shown in Fig. 3. (For interpretation of the references to color in this figure legend, the reader is referred to the web version of this article.)

RDFs presented above. In the same plots, we also present the form factors calculated for each aspect ratio. Fig. 7 shows the respective scattering intensities, with the insets showing the plots in log/log scale. The abcissae of all the plots are presented as QD so that the first peak in each structure factor is situated in the same range for all aspect ratios. Calculation of the structure factor at low Q is limited by the maximum distance sampled in the radial distribution function, $Q_{min} = 2\pi/r_{max}$, which in turn is limited by the size of the

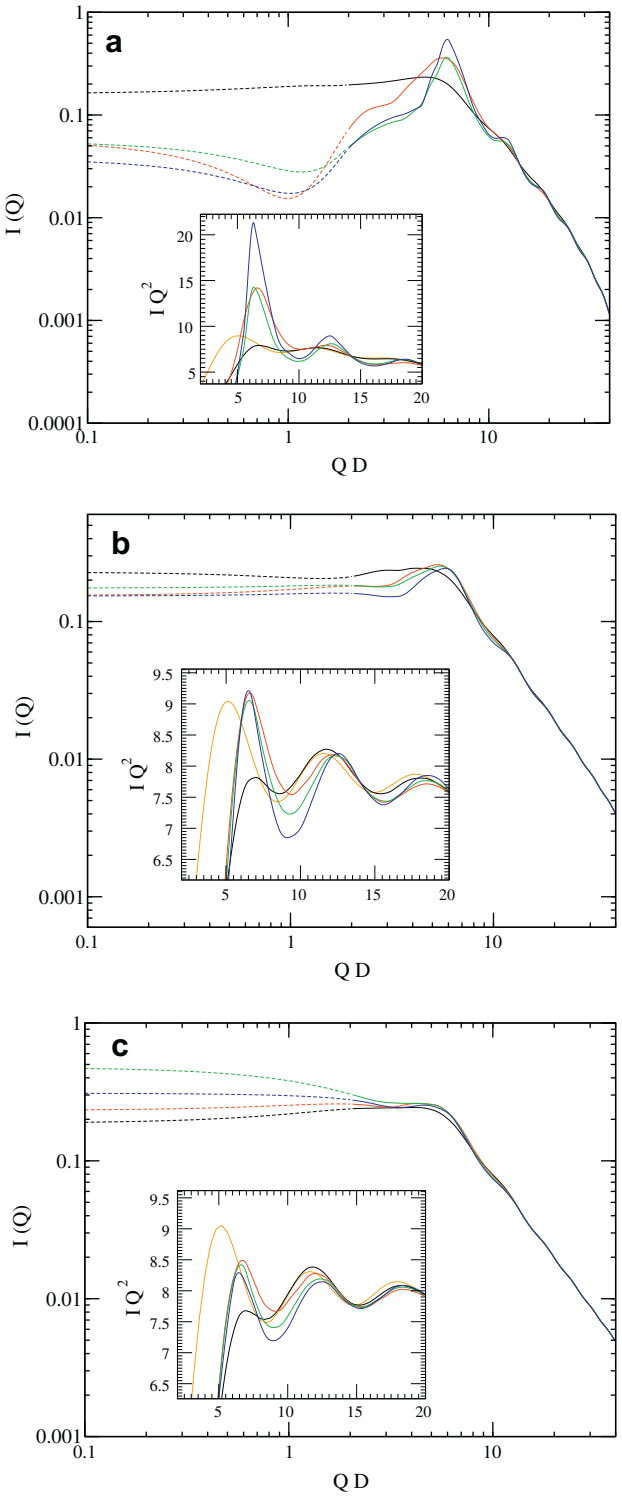

Fig. 7. Predicted scattering intensities corresponding to the structure factors of Fig. 6 keeping colors consistent. The insets show the same plots with the intensity scaled by Q^2. (For interpretation of the references to color in this figure legend, the reader is referred to the web version of this article.)

system in the simulations. In our simulations the value of $Q_{min}D$ is always between 1 and 2. The value of the structure factor at $Q = 0$ is related to the isothermal compressibility, χ_T, of the system by

$$S(Q=0) = \rho\ \beta^{-1}\ \chi_T, \quad \chi_T = -\frac{1}{V}\left(\frac{\partial V}{\partial p}\right)_{N,T} \iff S(Q=0) = \left(\frac{\partial \rho}{\partial \beta p}\right)_{N,T} \tag{13}$$

where V is the volume, p is the pressure and $\beta = (k_B T)^{-1}$ with k_B as the Boltzmann constant and T as the temperature. The values of $S(Q = 0)$ presented in the plots were, therefore, independently calculated from the slopes of the equations of state, presented in Fig. 3. They were then used in the interpolation of the structure factors from the minimum value obtained from the RDFs to the limit of $Q = 0$.

For the isotropic phase at low density the structure factors in Fig. 6 are all very similar showing a very weak first peak, located near 7 QD, which corresponds to the sharp peak around $r/D = 1$ in the radial distribution $g(r)$ (see the previous section above). This means that pair correlations at low density have the same range and intensity independent of the aspect ratio of the platelets, as expected. The intensity of the first peak in the structure factor for the isotropic phase at the transition changes significantly with aspect ratio. The peaks are much more intense for $L/D = 0.1$ reflecting the higher degree of pair correlations in systems of thicker particles. Note that the first peak grows and widens significantly (see Figs. 6 and 7) as the isotropic phase is approaching the I–N transition, but then narrows in the nematic phase at the transition, after which it increases in intensity, but not in width, with increasing concentration. The slight change in the position of the first peak has a similar evolution, as we increase the density, for all aspect ratios. The peak moves to lower Q as density increases, indicating increasingly long-range correlations. Our structure factors show the same features as the ones calculated from RISM and PRISM theories [12] for low density isotropic phases ($\rho D^3 < 2.8$) of platelets with aspect ratio $L/D = 0.1$ and 0.04. The intensity of the first peak is approximately the same as in our work but the peak positions in that work are systematically moved to higher Q values (by about 6% at $\rho D^3 = 1.4$) and the compressibilities are significantly higher. This is expected because the equations of state from these theories start to differ from the ones calculated by our MC simulations for $\rho D^3 > 0.7$ showing systematically lower pressures for higher densities and thus higher compressibility.

The order of the peak positions is reversed in the intensity plots compared to the structure factor plots, see Fig. 7, where the first peak moves from lower to higher Q values as the density increases. Also, in the intensity plots only the first peak is particularly visible, either on linear or log scale plots. Another feature of the intensity plots that can be useful for identification of the morphology is the evolution of $I(Q)$ at low Q values. For thick particles ($L/D = 0.1$, see Fig. 7a) the intensity, in the limit of $Q \to 0$, decreases with increasing density, as expected in dispersions of isotropic particles. For thin particles ($L/D = 0.01$, see Fig. 7c) the intensity, in the limit $Q \to 0$, somewhat increases with increasing density in the isotropic phase. Surprisingly, it then jumps to higher values (almost three times) when going from the isotropic to the nematic phase at the I–N transition. The intensity at the limit of $Q \to 0$ then decreases with increasing density in the nematic phase. This behavior for $I(Q = 0)$ is a direct consequence of the shape of the equations of state presented in Fig. 3. In order to estimate intensities at the limit of $Q \to 0$, measurements need to be done at sufficiently small scattering angles (corresponding to Q values to the left of the dashed line in Fig. 8) and extrapolated to $Q = 0$. As can be seen from Fig. 8, the required range of Q values would be accessible by SLS measurements. We note that in scattering experiments samples are often enclosed between two parallel plates, which could induce additional platelet ordering effects, especially when the gap between the plates becomes very small. Since this might possibly influence the observed bulk phase behavior, it is advisable to check for boundary effects in experimental measurements, for example, by using cells of variable shape or thickness if possible.

To summarize, for thicker platelets ($L/D = 0.1$), the morphology around the I–N transition can be well determined from the height and width of the first peak near 7 DQ and the presence of the

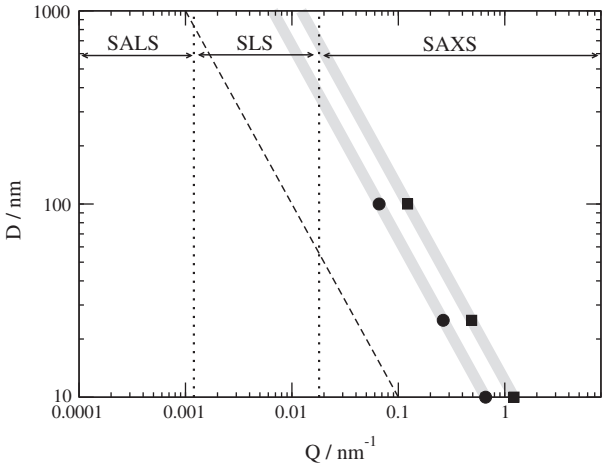

Fig. 8. Typical scattering ranges of different techniques (separated by dotted lines) and the first two peak positions (circles and squares) for aspect ratios $L/D = 0.1$, 0.04 and 0.01 (with $L = 1$ nm). The thick gray lines are a linear fit to the peak positions. The dashed line corresponds to $QD = 1$.

corresponding second peak in the scattering intensity pattern. These peaks are to be found in the range of Q values accessible by SAXS measurements for typical values of colloidal platelet diameters, as can be seen in Fig. 8. However, very short range close distance correlations indicative of a caging effect observed as a peak in $g(r)$ peak around $r/D = 0.1$ would be all but undetectable from scattering measurements. The scattering intensities, at the limit of $Q \rightarrow 0$, near the transition are significantly lower than that of a dilute isotropic phase, but they do not show any further changes upon entering the nematic phase region. On the other hand, for thinner platelets ($L/D = 0.01$), normalized intensity differences between isotropic and nematic phases appear to be barely observable from peak magnitudes or shapes and perhaps might be just picked up from IQ^2 plots (as shown on the inset in Fig. 7). However, low angle scattering intensities (as $Q \rightarrow 0$) show pronounced dependence on the concentration near the transition and should be useful in identification of the structural transition from scattering experiments.

4. Final remarks

We studied the isotropic–nematic phase transition of hard discotic particles with Monte-Carlo simulations for a range of aspect ratios not previously studied. Our results, suggest this transition is very weak indeed for aspect ratios <0.04, to the point that we cannot be sure if the transition exists for lower aspect ratios or whether it is terminated by a critical point. Although earlier work [15,14,17] has revealed the transition to be rather weak, it has previously always been thought to be a weak first-order transition. We also observe a minimum in the density of coexisting phases around the same aspect ratio, which might be observable in experiments on dispersions of discotic particles whose aspect ratio can be adjusted by chemical means.

The main focus of this work is on structural properties of each phase, especially close to coexistence, to determine if these phases can be distinguished experimentally using techniques such as light or X-ray scattering. We find from our simulations that for thicker disks (larger aspect ratios) certain peaks in the static structure factor should be observable experimentally and are characteristic of each phase. However, these peaks diminish for thin disks (small aspect ratios) to the point that they are likely to be unobservable above experimental noise. Instead, for smaller aspect ratios where these peaks become less prominent, low Q normalized scattering intensities, which also reflect the behavior of the equation of state, can be used to detect the I–N transition.

Our motivation for this work is to provide data and techniques for interpretation of experimental scattering data of isotropic and nematic phases of discotic nanoparticle dispersions, and the inverse problem of calibrating simulation models using experimental scattering data. However, our simulations correspond only to the high temperature limit of some widely studied popular systems, such as clay dispersions, and mono-dispersity was assumed with respect to particle size. Consequently, these results should be used with some caution. Most likely, they will be useful for dispersions involving synthetic discotic mesogens whose size can be carefully controlled and is relatively monodisperse, such as Laponite (a hectorite clay [28,29]) or certain oxides, such as Gibbsite [24,46]. The effect of polydispersity on phase behavior of discotic systems has been studied previously by Bates and Frenkel [17], who found that polydispersity in diameter enlarges the coexistence region and that, at the transition, there is partial segregation between phases. That is, there is a higher concentration of particles of larger diameter in the nematic phase. However, to our knowledge there are no studies on the effect of polydispersity on structural properties of hard disks. At the very least, one can expect size polydispersity to further reduce the significance of certain peaks in the structure factors, making identification of each phase even more problematic. At lower temperatures we expect other interactions, especially of electrostatic origin for clays, to become dominant, and alter the behavior of these systems. For example, earlier work [47] indicates that at ambient conditions an electric dipole in the plane of Laponite particles is important and drives aggregation of Laponite to form complex fractal-like structures resembling a defective dipolar fluid.

Acknowledgments

The authors gratefully acknowledge support from the EPSRC and AWE, with Grant EP/E049222/1. The authors are especially grateful to Professor Richard Pethrick and Dr. John Liggat for insightful discussions on the subject of this work.

Appendix A

A.1. Definition of the cut-sphere model

A geometrical object generated by cutting a sphere with two parallel planes. The parameters that describe the model are just the diameter of the sphere (D_s) and the thickness (L), given by distance between the planes. The circles on top and bottom of the cut-sphere, produced by the intersection of the planes and the sphere, will be named as "cap"s and the spherical surface will be named as "rim".

Secondary parameters used here are:

$D_{2s} = D_s/2$
$L_2 = L/2$
$D_{2c} = \sqrt{D_{2s}^2 - L_2^2} \rightarrow$ the radius of a cap
$\mathbf{n} \rightarrow$ the unit vector normal to the caps
$\mathbf{C}_s \rightarrow$ the center of the sphere
$\mathbf{C}_{c1} = \mathbf{C}_s + L_2\mathbf{n}$ and $\mathbf{C}_{c2} = \mathbf{C}_s - L_2\mathbf{n} \rightarrow$ centers of the caps
$\alpha \rightarrow$ the arc length of the rim
$\alpha_2 = \alpha/2$ with $\sin(\alpha_2) = L_2/D_{2s}$

A configuration, regarding a pair of cut-spheres (i, j), is completely defined by the vector

$$\mathbf{r}_{ij} = \mathbf{C}_{s,j} - \mathbf{C}_{s,i} \tag{14}$$

and the vectors $\mathbf{n}_i$ and $\mathbf{n}_j$.

A.2. Tests for overlapping of cut-spheres

A.2.1. Overlapping of spheres

The spheres cannot overlap if

$$|\mathbf{r}_{ij}| > D_s \tag{15}$$

and therefore the cut-spheres do not overlap also.

A.2.2. Quasi-parallel cut-spheres

The caps are parallel (within numerical precision in use) if

$$|\mathbf{n}_i \times \mathbf{n}_j| < \delta \tag{16}$$

or if

$$|\mathbf{n}_i \cdot \mathbf{n}_j| - 1 < \delta \tag{17}$$

where δ is a parameter (very close to zero) defining the precision within which the disks are considered to be parallel.

If the caps are parallel, then the cut-spheres overlap if

$$|\mathbf{r}_{ij} \cdot \mathbf{n}| < L \quad \wedge \quad |\mathbf{r}_{ij}| < D_s \tag{18}$$

where the left term takes in account the distance between the caps and the right term is the sphere interaction test (same as Eq. (15)).

A.2.3. Rim-rim overlapping

Rim-rim overlapping is similar to sphere overlapping. The additional condition is that the $\mathbf{r}_{ij}$, $\mathbf{n}_i$ and $\mathbf{n}_j$ are in a configuration which assures only rim-rim contact. Considering γ, the angle between $\mathbf{n}$ and $\mathbf{r}_{ij}$, defined by

$$\cos(\gamma) = \frac{\mathbf{n} \cdot \mathbf{r}_{ij}}{|\mathbf{r}_{ij}|} \tag{19}$$

then the condition for a rim-rim approach is

$$\left|\frac{\pi}{2} - \gamma_i\right| < \alpha_{2i} \quad \wedge \quad \left|\frac{\pi}{2} - \gamma_j\right| < \alpha_{2j} \tag{20}$$

If this condition is true, then the condition of Eq. (15) is used to decide if the cut-spheres are overlapping.

A.2.4. Cap-cap overlapping

For cap-cap overlapping the planes of the caps must intersect in a line which, in its turn, has to intersect both caps at the same time, forming chords. Further to that, those cords have to overlap. A general cap-cap overlapping is presented. It will be used for the four possible interactions. The first step is to determine the line of intersection. We write the equation the plane of a cap as

$$\mathbf{n} \cdot \mathbf{P} + d = 0, \quad d = -\mathbf{n} \cdot \mathbf{C}_c, \quad \mathbf{P} = (x, y, z), \quad \mathbf{n} = (a, b, c). \tag{21}$$

The director vector of the line is then

$$\mathbf{u}' = \mathbf{n}_i \times \mathbf{n}_j \quad \text{or} \quad \mathbf{u} = \frac{\mathbf{n}_i \times \mathbf{n}_j}{|\mathbf{n}_i \times \mathbf{n}_j|}. \tag{22}$$

For the complete definition of the line we still need a point lying in it. As the system of equations formed by the two planes

$$\begin{cases} \mathbf{n}_i \cdot \mathbf{P} + d_i = 0 \\ \mathbf{n}_j \cdot \mathbf{P} + d_j = 0 \end{cases} \tag{23}$$

is indeterminate, we have to find a particular solution. One way is to take the largest, in modulus, coordinate of $\mathbf{u}$ and make it equal to zero on the equations. If we chose, e.g., z, then the point in the line is given by

$$\mathbf{P}_{0(z)} = \frac{\left(\begin{vmatrix} b_i & b_j \\ d_i & d_j \end{vmatrix}, -\begin{vmatrix} a_i & a_j \\ d_i & d_j \end{vmatrix}, 0\right)}{\begin{vmatrix} a_i & a_j \\ b_i & b_j \end{vmatrix} = z \text{ component of } \mathbf{u}'} \tag{24}$$

and the line is

$$\mathbf{P} = \mathbf{P}_0 + t\mathbf{u}. \tag{25}$$

For the other coordinates, the solutions for $\mathbf{P}_0$ are:

$$\mathbf{P}_{0(x)} = \frac{\left(0, \begin{vmatrix} c_i & c_j \\ d_i & d_j \end{vmatrix}, -\begin{vmatrix} b_i & b_j \\ d_i & d_j \end{vmatrix}\right)}{\begin{vmatrix} b_i & b_j \\ c_i & c_j \end{vmatrix} = x \text{ component of } \mathbf{u}'} \tag{26}$$

$$\mathbf{P}_{0(y)} = \frac{\left(-\begin{vmatrix} c_i & c_j \\ d_i & d_j \end{vmatrix}, 0, \begin{vmatrix} a_i & a_j \\ d_i & d_j \end{vmatrix}\right)}{-\begin{vmatrix} a_i & a_j \\ c_i & c_j \end{vmatrix} = y \text{ component of } \mathbf{u}'} \tag{27}$$

We then calculate the minimum distance, l_m, from the center of each cap to that line by first finding the point of the line which is nearer to the center of the cap:

$$(\mathbf{P}_l - \mathbf{C}_c) \cdot \mathbf{u} = 0 \Rightarrow t = -\mathbf{u} \cdot (\mathbf{P}_0 - \mathbf{C}_c) \tag{28}$$

$$l_m = |\mathbf{P}_l - \mathbf{C}_c| \tag{29}$$

with t specifying the point $\mathbf{P}_l$ through Eq. (25). Now we can see that the caps do not intersect if the condition

$$l_{mi} > D_{2c} \quad \vee \quad l_{mj} > D_{2c} \tag{30}$$

holds true. Furthermore, only if the negative of this condition is true, then there can be cap-cap overlapping:

$$l_{mi} < D_{2c} \quad \wedge \quad l_{mj} < D_{2c}. \tag{31}$$

To finalize the test we have to see if the chords are superimposed, which happens if

$$|t_i - t_j| < \sqrt{D_{2ci}^2 - l_{mi}^2} + \sqrt{D_{2cj}^2 - l_{mj}^2} \tag{32}$$

where the right member accounts for the half-lengths of each chord.

A.2.5. "in cylinder" Overlapping

If one of the cut-spheres center lies inside the cylinder defined by the caps of the other cut-sphere the overlapping tests are simpler.

Cut-sphere j lies inside the cylinder of cut-sphere i if

$$l_h < D_{2ci} \tag{33}$$

where l_h is the "horizontal" distance between cut-spheres, defined as

$$l_h = \sqrt{r_{ij}^2 - (\mathbf{r}_{ij} \cdot \mathbf{n}_i)^2}. \tag{34}$$

In this case it is simple to choose the interacting cap of cut-sphere i. We have

$$\begin{aligned} &\mathbf{n}_i \cdot \mathbf{r}_{ij} < 0 \quad \Rightarrow \quad s_i = -L_{2i} \\ &\mathbf{n}_i \cdot \mathbf{r}_{ij} \geqslant 0 \quad \Rightarrow \quad s_i = +L_{2i} \\ &\mathbf{C}_{ci} = \mathbf{r}_i + s_i \cdot \mathbf{n}_i \end{aligned} \tag{35}$$

Cap-cap overlap is possible if the projection of D_{2cj} on $\mathbf{n}_i$ is larger than the "vertical" distance between the caps of cut-sphere j and the cap of cut-sphere i, that is:

$$D_{2cj}\cdot\sqrt{1-\left(\mathbf{n}_i\cdot\mathbf{n}_j\right)^2} > |(\mathbf{C}_{c1j}-\mathbf{C}_{ci})\cdot\mathbf{n}_i| \quad \wedge D_{2cj} \cdot\sqrt{1-\left(\mathbf{n}_i\cdot\mathbf{n}_j\right)^2} > |(\mathbf{C}_{c2j}-\mathbf{C}_{ci})\cdot\mathbf{n}_i| \tag{36}$$

In this case we can use the cap-cap overlapping test for the intersections between the two caps of cut-sphere j and the cap of cut-sphere i.

Another possibility is the rim of cut-sphere j overlapping with the cap of cut-sphere i. This happens if

$$|\mathbf{n}_i\cdot\mathbf{n}_j| < \sin(\alpha_{2j}) \quad \wedge \quad |(\mathbf{C}_{sj}-\mathbf{C}_{ci})\cdot\mathbf{n}_i| < D_{2sj}. \tag{37}$$

Finally, an overlap always occurs if the "vertical" distance between the center is less than the sum of the half-thicknesses of the cut-spheres,

$$|\mathbf{r}_{ij}\cdot\mathbf{n}_i| < L_{2i}+L_{2j} \tag{38}$$

A.2.6. Cap-rim overlapping

Cap-rim overlaps are detected by first determining if the cap-plane of one cut-sphere intersects the sphere of the other cut-sphere. The distance from the center of cut-sphere j to the plane of the cap of cut-sphere i is

$$l_{sj,ci} = \mathbf{n}_i\cdot(\mathbf{C}_{sj}-\mathbf{C}_{ci}). \tag{39}$$

The cap-plane cuts the sphere if

$$|l_{sj,ci}| < D_{2sj} \tag{40}$$

If this condition is true we then need to see if the cap, and the circle from the cut, overlap. The center of the cut is given by

$$\mathbf{P}_{\text{circ}} = \mathbf{C}_{sj} - l_{sj,ci}\,\mathbf{n}_i \tag{41}$$

and radius

$$D_{2\text{circ}} = \sqrt{D_{2sj}^2 - l_{sj,ci}^2}.$$

Now we test for a circle overlap, which happens if the condition

$$|\mathbf{P}_{\text{circ}}-\mathbf{C}_{ci}| < D_{2ci}+D_{2\text{circ}} \tag{42}$$

holds true. The overlap between the circles corresponds to a cap-rim overlap only if the two points resulting from the circumferences intersection are contained in the sphere surface section between the planes of the cut-sphere j. A simpler test consists of calculating the middle point between the two intersection points and seeing if it lies between the planes of cut-sphere j. The middle-point of the intersection is given by

$$\mathbf{P}_{\text{isec}} = \mathbf{C}_{ci} + \frac{(\mathbf{P}_{\text{circ}}-\mathbf{C}_{ci})\cdot\left(D_{2ci}^2 - D_{2\text{circ}}^2 + |\mathbf{P}_{\text{circ}}-\mathbf{C}_{ci}|^2\right)}{2|\mathbf{P}_{\text{circ}}-\mathbf{C}_{ci}|^2} \tag{43}$$

and it lies between the planes of cut-sphere j if

$$|(\mathbf{P}_{\text{isec}}-\mathbf{C}_{sj})\cdot\mathbf{n}_j| < L_{2j}.$$

Note that this test does not take into account the cap-rim overlaps where the circle resulting from the cut is inside the cap. This situation is considered in the "in cylinder" overlapping case.

A.3. General algorithm

The tests described above must be assembled in a logical sequence that guarantees a correct result for the cut-spheres interaction. The tests are exclusive, meaning that if one gives positive for overlap the sequence ends immediately. Overall, the proposed sequence is:

1. Start by the simpler tests: overlapping of spheres, quasi-parallel cut-spheres and rim-rim overlapping.
2. Detect a possible "in cylinder" situation. If confirmed, perform the cap-cap test and the cap-rim test.
3. Perform test for cap-cap overlapping for the four possible combinations of cap-cap intersection.
4. Perform the test for cap-rim overlapping for the four possible cases.

This is just a proposed sequence and it is not unique. Also, concerning the implementation, there are a number of ways of organizing the operations in the tests themselves that can improve the algorithm computational performance.

References

[1] E. Manias, Nature Mater. 6 (2007) 9.
[2] S. Pavlidou, C. Papaspyrides, Prog. Polym. Sci. 33 (2008) 1119.
[3] B. Chen, J.R.G. Evans, H.C. Greenwell, P. Boulet, P.V. Coveney, A.A. Bowden, A. Whiting, Chem. Soc. Rev. 37 (2008) 568.
[4] D. Paul, L. Robeson, Polymer 49 (2008) 3187.
[5] S. Stankovich, D. Dikin, G. Dommett, K. Kohlhaas, E. Zimney, E. Stach, R. Piner, S. Nguyen, R. Ruoff, Nature 442 (2006) 282.
[6] D. Konatham, A. Striolo, Nano Lett. 8 (2008) 4630.
[7] Y. Liang, D. Wu, X. Feng, K. Mullen, Adv. Mater. 21 (2009) 1679.
[8] H. Viet, V. Tran, T. Nguyen-Phan, D. Hai, E. Kim, S. Hur, E. Shin, S. Kim, J. Chung, Chem. Comm. 46 (2010) 4375.
[9] D. Li, M. Muller, S. Gilje, R. Kaner, G. Wallace, Nature Nanotech. 3 (2008) 101.
[10] M. Dijkstra, R. van Roij, R. Evans, J. Chem. Phys. 113 (2000) 4799.
[11] S. Kutter, J.P. Hansen, M. Sprik, E. Boek, J. Chem. Phys. 112 (2000) 311.
[12] D. Costa, J. Hansen, L. Harnau, Mol. Phys. 103 (2005) 1917.
[13] D. Chakrabarti, D.J. Wales, Phys. Rev. E 77 (2008) 051709.
[14] J.A.C. Veerman, D. Frenkel, Phys. Rev. A 45 (1992) 5632.
[15] D. Frenkel, R. Eppenga, Mol. Phys. 52 (1984) 1303.
[16] M.A. Bates, J. Chem. Phys. 111 (1999) 1732.
[17] M.A. Bates, D. Frenkel, J. Chem. Phys. 110 (1999) 6553.
[18] A. Chamoux, A. Perera, J. Chem. Phys. 108 (1998) 8172.
[19] X. You, A.Y. Vlasov, A.J. Masters, J. Chem. Phys. 123 (2005) 034510.
[20] A. Esztermann, H. Reich, M. Schmidt, Phys. Rev. E 73 (2006) 011409.
[21] D. Cheung, L. Anton, M. Allen, A. Masters, J. Phillips, M. Schmidt, Phys. Rev. E 78 (2008) 041201.
[22] D.L. Cheung, L. Anton, M.P. Allen, A.J. Masters, Comp. Phys. Comm. 179 (2008) 61.
[23] D. van der Beek, A. Petukhov, S. Oversteegen, G. Vroege, H. Lekkerkerker, Eur. Phys. J.E 16 (2005) 253.
[24] M. Mourad, D. Byelov, A. Petukhov, D. de Winter, A. Verkleij, H. Lekkerkerker, J. Phys. Chem. B 113 (2009) 11604.
[25] P. Sandkuhler, M. Lattuada, H. Wu, J. Sefcik, M. Morbidelli, Adv. Colloid Interface Sci. 113 (2005) 65.
[26] M. Soos, J. Sefcik, M. Morbidelli, Chem. Eng. Sci. 61 (2006) 2349.
[27] A. Cadene, S. Durand-Vidal, P. Turq, J. Brendle, J. Colloid Interface Sci. 285 (2005) 719.
[28] E. Balnois, S. Durand-Vidal, P. Levitz, Langmuir 19 (2003) 6633.
[29] E.S.H. Leach, A. Hopkinson, K. Franklin, J. van Duijneveldt, Langmuir 21 (2005) 3821.
[30] D. van der Beek, T. Schilling, H. Lekkerkerker, J. Chem. Phys. 121 (2004) 5423.
[31] F. van der Kooij, K. Kassapidou, H. Lekkerkerker, Nature 406 (2000) 868.
[32] M. Allen, G. Evans, D. Frenkel, B. Mulder, Hard convex body fluids, Advances in Chemical Physics, vol. 86, John Wiley & Sons Inc., 1993.
[33] D. Frenkel, B. Smit, Understanding Molecular Simulations: From Algorithms to Applications, 2nd ed., Academic Press, 2002.
[34] V.I. Harismiadis, J. Vorholz, A.Z. Panagiotopoulos, J. Chem. Phys. 105 (1996) 8469.
[35] E. de Miguel, G. Jackson, J. Chem. Phys. 125 (2006) 164109.
[36] M. Piñeiro, A. Galindo, A. Parry, Soft Matter 3 (2007) 768.
[37] R.P.S. Fartaria, M.B. Sweatman, Chem. Phys. Lett. 478 (2009) 150.
[38] J.P. Hansen, I.R. McDonald, Theory of Simple Liquids, 2nd ed., Elsevier Ltd., London, UK, 1986.
[39] A. Mourchid, A. Delville, P. Levitz, Faraday Discuss. 101 (1995) 275.
[40] F.M. v. d. Kooij, H.N.W. Lekkerkerker, J. Phys. Chem. B 102 (1998) 7829.
[41] S. Singh, Phys. Rep. 324 (2000) 107.
[42] F.v.d. Kooij, D.v.d. Beek, H.N.W. Lekkerkerker, J. Phys. Chem. B 105 (2001) 1696.
[43] J. Errington, Phys. Rev. E 67 (2003) 012102.
[44] R.A. Vaia, W.D. Liu, H. Koerner, J. Polym. Sci. B 41 (2003) 3214.
[45] L. Harnau, Mol. Phys. 106 (2008) 1975.
[46] J. Wijnhoven, D. van't Zand, D. van der Beek, H. Lekkerkerker, Langmuir 21 (2005) 10422.
[47] R. Fartaria, N. Javid, R.A. Pethrick, J.J. Liggat, J. Sefcik, M.B. Sweatman, Soft Matter 7 (2011) 9157.